Optics Communications 284 (2011) 398–404

Contents lists available at ScienceDirect

Optics Communications

journal homepage: www.elsevier.com/locate/optcom

Optimal performances of a mode-locking technique: Theoretical and experimental investigations of the frequency-doubling nonlinear mirror

A.A. Mani [a,*], D. Lis [b], Y. Caudano [b], P.A. Thiry [b], A. Peremans [b]

[a] Atomic Energy Commission of Syria, P.O. Box 6091, Damascus, Syria
[b] Research Centre in Physics of Matter and Radiation, University of Namur (FUNDP), 61 rue de Bruxelles, B-5000 Namur, Belgium

ARTICLE INFO

Article history:
Received 21 January 2010
Received in revised form 29 April 2010
Accepted 29 August 2010

Keywords:
Frequency-doubling nonlinear mirror
Mode-locking
Picosecond
Nd:YAG laser

ABSTRACT

We present a detailed analysis of the mode-locker consisting of a nonlinear crystal and a dichroic mirror, introduced by Stankov and known as the frequency-doubling nonlinear mirror (FDNLM). Our aim is to determine optimal values for two physical parameters: the *conversion efficiency* η_0 of the nonlinear crystal, and the *reflection coefficient* R_ω of the output mirror. The optimization is based on a set of three figures of merit: the *reflected intensity*, the *pulse shortening ratio* and the *Gaussian shape factor*, which are combined to yield a final *decision factor*. Experimental investigations of η_0 and R_ω carried out using a FDNLM mode-locked Nd:YAG laser show good agreement with the theoretical predictions. In addition, a comparative study with other available experimental results is presented. This work demonstrates the capacity of this method to evaluate the best performance of this mode-locking not only for the steady-state pulse domain but also in the transient one.

1. Introduction

Over the last decades the mode-locking principle has widely opened the road for generating ultra short laser pulses in both the picosecond and femtosecond time scales. Indeed all-solid-state mode-locking techniques such as additive-pulse mode-locking (APM), semiconductor saturable asbsorber mirror (SESAM), soliton mode-locking, saturable Bragg reflector (SBR), and Kerr lens mode-locking (KLM) have attracted more consideration than other techniques based on organic dyes, because of their shot-to-shot and day-to-day stabilities, very fast responses, and self-starting ability [1,2].

The frequency-doubling nonlinear mirror (FDNLM) mode-locker, originally proposed by Stankov consists of a nonlinear crystal coupled to a dichroic mirror. Its additional advantages over the aforementioned techniques are the following: it can provide passive *negative* as well as *positive* mode-locking and it can be applied over a wide spectral range from infrared to visible where many nonlinear crystals are available [3–7].

The performances of the FDNLM to generate mode-locked laser pulses have been demonstrated in many works, not only for continuous pulse-train lasers (CPT), (usually abbreviated by cw, not to be confused with continuous-wave lasers) but also for pulsed pulse-train lasers (PPT) [3,4,8–10]. The latter case generally corresponds to flashlamp-pumped lasers that usually generate more energetic pulses than CPT ones. Recently optical pulses as short as 12 ps with a good shot-to-shot stability have been generated from a flashlamp-pumped Nd:YAG laser. This laser setup combines on the one side, active mode-locking by using an acousto-optic mode-locker (AOML) and on the other side both passive-positive and -negative mode-locking by using a FDNLM and a two-photon absorber (TPA) respectively [11,12]. That configuration has been successfully integrated into a sum-frequency generation spectrometer in order to probe molecular monolayers deposited on metallic surfaces [11,13].

Alongside the running experiments, the pulse shortening mechanism of the FDNLM has been described by Stankov by means of a simple theoretical model where the device reflection is represented by an intensity-dependent nonlinear reflection coefficient [14]. Later an analytical solution has been derived by Barr for the steady-state condition in the case of pulse propagation inside a laser cavity containing both an AOML and a FDNLM [15]. Note that the previous condition can be reached after a large number of pulse round trips inside the laser cavity which is appropriate to describe the function of FDNLM for continuous pulse-train lasers mode-locking. More complicated numerical models based on coupled wave equations for each oscillating mode have been developed in many works to describe the transient behavior of the optical pulse inside a laser oscillator actively and passively mode-locked by an AOML and by a FDNLM respectively, which turns to be convenient to simulate the mode-locking process in flashlamp-pumped lasers [16–23].

However, as one may notice, simulating oscillators that are actively as well as passively mode-locked with both passive-positive and -negative mode-locking using a FDNLM and TPA components respectively, becomes a cumbersome task especially for the determination of the physical parameters involved. In our opinion, this

* Corresponding author. Tel.: +96 3112132580; fax: +96 3116112289.
E-mail address: scientific3@aec.org.sy (A.A. Mani).

0030-4018/$ – see front matter © 2010 Elsevier B.V. All rights reserved.
doi:10.1016/j.optcom.2010.08.071

difficulty accounts for the fact that rather than focusing on post-model analysis, all the aforementioned works investigate complicated analytical or numerical models, often limited to the pulse shortening ratio (PSR) and to the reflected intensity (I_r) (called the reflected pulse power in Ref. [20]) as the figures of merit of the FDLNM performances. In Ref. [21], the variations of nonlinear reflectivity, reflected energy and pulse lengthening ratio, are used with a new parameter called "steadiness" to describe the effect of the single-pass group delay in the crystal. Furthermore, in Ref. [22], the FDNLM nonlinear reflectivity is used with an additional parameter named "phase mismatch". Note that steadiness and phase mismatch could become important parameters and introduce additional complexity when the nonlinear crystal is relatively long as it is the case in Refs. [21] and [22] where LBO and $LiIO_3$ crystals of 15 and 30 mm were used. In our experiments relatively thin crystals in the range of 2 to 4 mm were used in order to avoid complexities and to select only two basic parameters, i.e. the dichroic mirror reflectivity R_ω and the second harmonic peak-power conversion efficiency η_0 as will be shown in the forthcoming sections.

In this work we present an extension of the Stankov model by defining a set of three functions of the two principal parameters of the FDNLM: the peak-power conversion efficiency η_0 of the nonlinear crystal, and the reflection coefficient R_ω of the mirror. These three running factors or figures of merit are: the reflected intensity (I_r), the pulse shortening ratio (PSR) and the Gaussian shape factor (GSF). The final decision factor that results from a weighted product of the three figures of merit yields best values for η_0 and R_ω and thus provides optimal performances of the FDNLM, as well as better understanding of the device functioning. In order to verify our predictions, experimental measurements have been carried out with a flashlamp-pumped Nd:YAG laser actively and passively mode-locked by using an AOML and a FDNLM combined with a TPA.

2. Theoretical investigation

2.1. The frequency-doubling nonlinear mirror (FDNLM)

The general configuration of a FDNLM is depicted in Fig. 1, in which a second harmonic generation (SHG) crystal is coupled to a dichroic mirror with a proper separation between them. In the first stage the fundamental wavelength (FW) pulse I_i passes through the SHG crystal (optimized for type I interaction) generating a pulse at the second harmonic (SH) with intensity proportional to the conversion efficiency of the crystal, η. At this stage special attention should be paid to the polarizations of interacting waves and to the crystal cut in order to maximize the second harmonic as shown on Fig. 1. The two pulses are then re-injected inside the crystal after being selectively reflected by the dichroic mirror that has reflection coefficient R_ω for the fundamental wavelength and $R_{2\omega}$ (≈ 1) for the second harmonic.

In the second stage, a down-conversion process takes place when the phase difference between the fundamental and the second harmonic, accumulated during propagation in air, reaches an odd multiple of π. The two passes through the crystal make this device similar to a mirror with an intensity-dependent reflection coefficient R_{NL}. In passive-positive action, the FDNLM reflects the high intensity part of the incident pulse more than the lower one, which leads to shortening the reflected pulse. The instantaneous reflection coefficient R_{NL} has been formulated by Stankov with respect to a normalized incident pulse intensity I_i as follows: [14]

$$R_{NL}(t) = B(t)\left\{1-\tanh^2\left[\sqrt{B(t)}\,\mathrm{atanh}\sqrt{\eta(t)}-\mathrm{atanh}\sqrt{\eta(t)/B(t)}\right]\right\} \quad (1)$$

with

$$B(t) = \eta(t) + [1-\eta(t)]R_\omega \quad \text{and} \quad \eta(t) = \tanh^2\left[\sqrt{I_i(t)}\,\mathrm{atanh}\sqrt{\eta_0}\right],$$

$$\text{for } \begin{matrix}\eta_0 \in [0,\,1[\\ R_\omega \in [0,\,1],\end{matrix}$$

where the two functions $\eta(t)$ and $B(t)$ represent the instantaneous second harmonic power conversion efficiency in the nonlinear crystal and the fraction of the total intensity (FW + SH) reflected by the dichroic mirror, respectively. From Eq. (1) one finds that R_{NL} is a function of time t and of the two principal parameters of the FDNLM, R_ω and η_0. η_0 is the power conversion efficiency $\eta(t)$ at the maximum of the incident pulse i.e. $\eta_0 = \eta(t=0)$. Nevertheless the expression of η_0 depends on the crystal characteristics and also on the incident intensity I_0:

$$\eta_0 = \tanh^2\left[\sqrt{\frac{8\pi^2 L^2\left|\chi_{eff}^{(2)}\right|^2 I_0}{(n_\omega^0)^3\lambda^2}}\right]. \quad (2)$$

$\chi_{eff}^{(2)}$ is the effective second-order susceptibility and n_ω^0 is the ordinary refractive index at the fundamental wavelength (λ) for the nonlinear crystal of length L. I_0 is the maximum intensity (peak intensity) of the injected pulse. The behavior of η_0 is represented in Fig. 2 as a function of I_0 for different crystal lengths in the case of β-barium borate (β-BBO cut at θ = 22.8 ° for type I interaction). The two dashed vertical lines shown on Fig. 2 indicate the estimated range of the intensity inside the cavity (determined by both the gain medium and the GaAs platelet inserted in the cavity as a TPA) in our experimental setup [10,11,13]. By rescaling Fig. 2 one can find η_0 for any different crystal types and irradiation intensities, and then find the corresponding crystal length that should be used in the laser oscillator. Noteworthy Eq. (2) is an approximation for an incident *plane* wave, which is not generally the case in experiments. However integrating the instantaneous conversion efficiency $\eta(t)$ over temporal profile and spatial distribution variations, as shown in Eq. (3), results in an *overall conversion efficiency* η_{oc} more adequate for comparison to experimental data. Table 1 shows the correspondence between the peak-power conversion efficiency η_o and the overall efficiency η_{oc} calculated for a

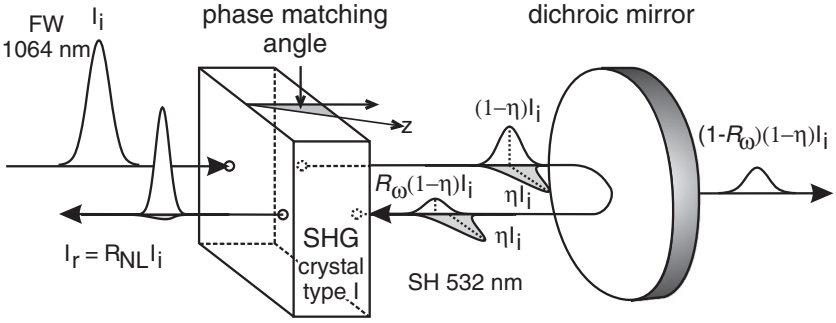

Fig. 1. Schematic view of the two passes into the frequency-doubling nonlinear crystal (see the text for more details).

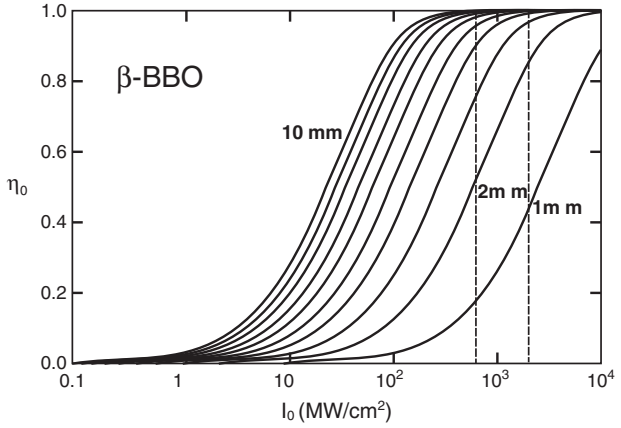

Fig. 2. Second harmonic peak-power conversion efficiency η_0 of the β-BBO crystal as a function of the incident FW intensity I_0 in MW/cm^2. The different curves correspond to 1, 2, 3, 4, 5, 6, 7, 8, 9 and 10 mm crystal lengths respectively from right to left. The two dashed vertical lines indicate the range of the estimated intensity inside the cavity of our experimental setup.

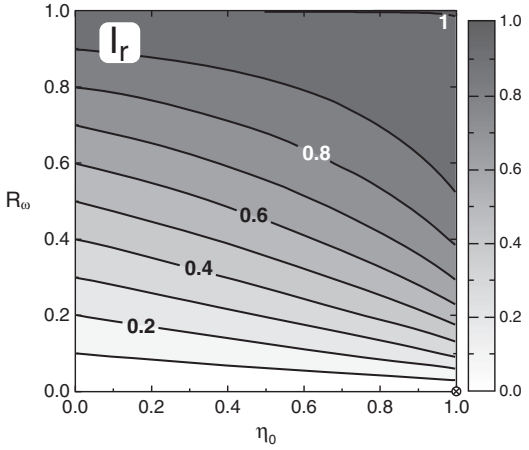

Fig. 3. Contour lines of the reflected peak intensity I_r as a function of the peak-power conversion coefficient η_0 (horizontal, the symbol ⊗ indicates the discontinuity at $\eta_0 = 1$) and reflection coefficient R_ω (vertical). The gray scale intensity of I_r is displayed on the right.

TEM_{00} mode with a Gaussian temporal profile. One can check from Table 1 that η_{oc} is always smaller than η_o.

$$\eta_{oc}(\eta_0) = \frac{\int_0^\infty \int_0^\infty \eta(r,t,\eta_0) I(t,r) r \; dr dt}{\int_0^\infty \int_0^\infty I(t,r) r \; dr dt} \tag{3}$$

with $I(t,r) = I(t)I(r) = \exp[-4\ln 2(t/\tau)^2]\exp[-2(r/w)^2]$ for TEM_{00}, where τ is the pulse width and w the beam waist. In this theoretical treatment, we mainly take a Gaussian temporal shape of the incident optical pulse $I_i(t) = \exp(-4t^2 \ln 2)$ with full width at half maximum (FWHM) equal to unity. Therefore, the instantaneous reflected pulse intensity $I_r(t)$ is given by:

$$I_r(t) = R_{NL}(t, \eta_0, R_\omega) I_i(t) \quad \text{for} \quad \eta_0 \in [0, 1[\quad \text{and} \quad R_\omega \in [0, 1]. \tag{4}$$

In the next sections we define a set of three figures of merit as functions of R_ω and η_0.

2.2. The reflected intensity (I_r)

As a first step, using the formalism described in the previous section, the map of the peak values of the reflected intensity I_r is calculated as a function of R_ω and η_0. The corresponding contour lines of I_r are drawn on Fig. 3 where one observes, as expected, that the maximum reflected intensity is obtained in the upper right corner of the graph for $R_\omega = 1$ and η_0 close to 1. Since Eq. (1) and consequently Eq. (4) have a discontinuity at $\eta_0 = 1$ —besides that, this value doesn't represent any practical physical situation — a circled cross symbol ⊗ is shown on η_0 axis at the value 1 in all figures from 3 to 7. In this case the last numerically calculated value of Eq. (1) is for $\eta_0 = 0.999$.

Table 1
Overall conversion efficiency η_{oc} versus peak-power conversion efficiency η_0 for a Gaussian temporal pulse and TEM_{00} mode.

η_0	η_{oc}
0.01	0.0036
0.10	0.037
0.25	0.096
0.50	0.21
0.80	0.42
0.95	0.62
0.99	0.75

2.3. The normalized pulse shortening ratio (PSR)

As a second step, we calculate the ratio between the FWHM of the instantaneous reflected intensity $I_r(t)$ and the incident one $I_i(t)$, which is called pulse shortening ratio (PSR). Contour lines of the normalized pulse shortening are drawn on Fig. 4 as a function of the reflection coefficient R_ω and of the peak-power conversion efficiency η_0. The normalization is performed as follows:

$$PSR(\eta_0, R_\omega)_{\text{normalized}} = \frac{PSR_{\max} - PSR(\eta_0, R_\omega)}{PSR_{\max} - PSR_{\min}}, \tag{5}$$

where the maximum and minimum values are taken over the entire variation range of η_0 and R_ω. In the case of a Gaussian pulse, those values are $PSR_{max} = 1$, $PSR_{min} = 0.836$ respectively. Hence the best efficient pulse shortening process is characterized by the minimum value PSR_{min} and consequently by the maximum value of the normalized pulse shortening ratio (equal to unity) that is being reached for $\eta_0 = 0.77$ and $R_\omega = 0$ as shown in Fig. 4. This latter outcome is not useful in practice because then as can be seen from Fig. 3, the reflected intensity I_r tends to zero, whereas the maximum reflected intensity is reached for very high values of R_ω.

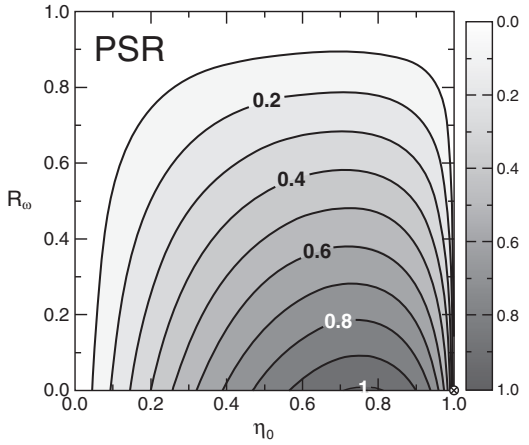

Fig. 4. Contour lines of the normalized pulse shortening ratio (PSR) as a function of peak-power conversion coefficient η_0 (horizontal, the symbol ⊗ indicates the discontinuity at $\eta_0 = 1$) and reflection coefficient R_ω (vertical). The gray scale intensity is displayed on the right.

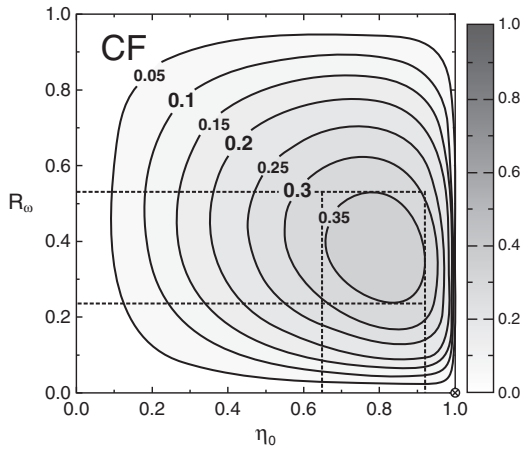

Fig. 5. Contour lines of the pulse compression factor CF described as a function of the peak-power conversion coefficient η_0 (horizontal, the symbol ⊗ indicates the discontinuity at $\eta_0=1$) and of the reflection coefficient R_ω (vertical). The gray scale intensity is displayed on the right.

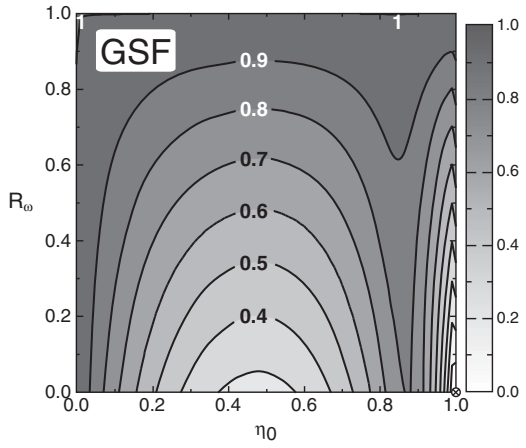

Fig. 6. Contour lines of the normalized Gaussian shape factor (GSF) as a function of the peak-power conversion coefficient η_0 (horizontal, the symbol ⊗ indicates the discontinuity at $\eta_0=1$) and of the reflection coefficient R_ω (vertical). The gray scale intensity is displayed on the right.

The shortcoming of the pulse shortening ratio leads to defining the compression factor (CF) of the pulse, i.e.:

$$CF(\eta_0,R_\omega)=PSR(\eta_0,R_\omega)_{\text{normalized}}\times I_r(\eta_0,R_\omega), \tag{6}$$

Note that the map of the reflected intensity is generally normalized because its maximum and minimum vales are equal to 1 and 0 respectively. Fig. 5 shows the contour lines of the compression factor with respect to η_0 and R_ω for a Gaussian incident pulse. Like the other factors the best performance of the compression process should be achieved for a compression factor equal to unity, which is not reachable by our device as shown in Fig. 5. The maximum value of the compression factor is about 0.35, obtained for η_0 in the range from 0.66 to 0.92 and R_ω from 0.23 to 0.54, which indicates the performance limit of the FDNLM as a pulse temporal compressor.

2.4. The normalized Gaussian shape factor (GSF)

So far, our choice for the basic parameters of the FDNLM did not take into account the detailed shape of the reflected pulse although it is an important factor for making a good oscillator, especially when the FDNLM is installed as the output coupler, i.e. the reflected and transmitted pulses will be deformed by the nonlinear reflection coefficient of the device. For that purpose, we define a new figure of merit called Gaussian shape factor (GSF) describing how much the reflected pulse is distorted from the original Gaussian shape. The value of the Gaussian shape factor is obtained by calculating the standard error value between the curve of the reflected pulse $I_r(t)$ and a Gaussian curve $I_G(t)$ that shares the same peak intensity and FWHM as given by the expression:

$$GSF=\sqrt{\frac{\sum_{n=1}^{N}[I_r(n)-I_G(n)]^2}{N-1}}, \tag{7}$$

where N is the number of points taken for each curve. As the pulse shape is symmetric around the zero point we take $N=100$ for only one side of the curve to guarantee a relative error smaller than 0.002%.

Then the normalized form of the Gaussian shape factor is given by:

$$GSF(\eta_0,R_\omega)_{\text{normalized}}=\frac{GSF_{\max}-GSF(\eta_0,R_\omega)}{GSF_{\max}-GSF_{\min}} \tag{8}$$

In the case of a Gaussian incident pulse, $GSF_{\max}=0.006$ and $GSF_{\min}=0$. The contour lines of the calculated normalized Gaussian shape factor are depicted on Fig. 6. As mentioned before, the best performance of the device operation is expected for the minimum Gaussian shape factor and consequently for the maximum of the normalized one (i.e. equal to one). The maximum is reached in the left and top boundaries of the map corresponding to unpractical situations when $\eta_0=0$ (i.e. no device at all) and $R_\omega=1$ (i.e. no output), respectively. Surprisingly normalized Gaussian shape factor values as high as 0.85 can be reached even for high η_0 values and moderate R_ω values that is very close to the best pulse temporal compression performance of the device. Thus following the trend of Fig. 6, we can improve the normalized GSF by a factor of 3, while getting higher compression.

2.5. The decision factor (DF)

In order to decide about the best η_0 and R_ω values, we need to assemble the three aforementioned factors in a new figure of merit called the decision factor (DF) expressed as the weighted product of the normalized pulse shortening ratio PSR, the reflected peak intensity I_r, and the normalized Gaussian shape factor GSF raised to the powers s, p and g, respectively, as follows:

$$DF(\eta_0,R_\omega)=[PSR(\eta_0,R_\omega)_{\text{normalized}}]^s\times[I_r(\eta_0,R_\omega)]^p\times[GSF(\eta_0,R_\omega)_{\text{normalized}}]^g. \tag{9}$$

The latter numerical exponents are introduced to show or to put emphasis on the different factors involved. Varying s, p, g over the useful interval from 1 to 3, will result in slightly different regions hence we only present the most significant maps in Fig. 7:

- In the upper left panel we show the calculated contour lines of the decision factor for $s=1, p=1, g=1$ (equal balancing between the three involved factors) for which one can readily conclude that the best theoretical operation of the FDNLM is situated in the *A* region, where $\eta_0\in[0.77, 0.88]$ and $R_\omega\in[0.25, 0.53]$.
- Furthermore putting the emphasis only on the shortening mechanism by setting $s=3$ (with $p=g=1$), will result in displacing the region towards lower R_ω values, as shown in the upper right panel. Thus, the best performance is located in the region *B*, where $\eta_0\in[0.78, 0.88]$ and $R_\omega\in[0.15, 0.28]$. This latter situation is more appropriate for PPT lasers and especially for flashlamp-pumped lasers, in which efficient pulse compression is

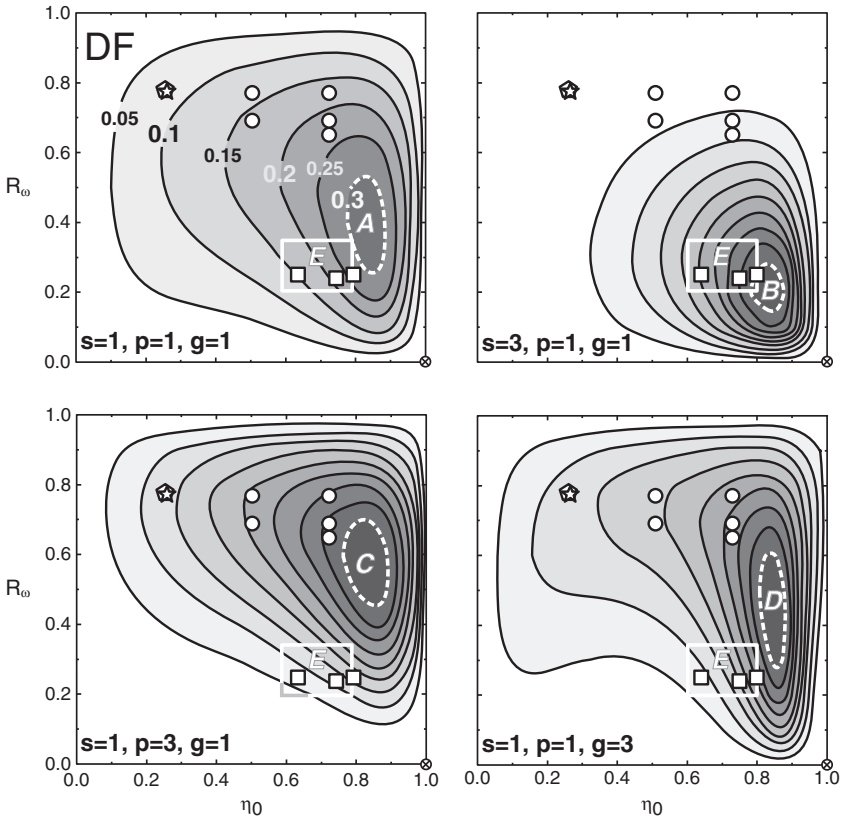

Fig. 7. Contour lines of the decision factor (DF) as a function of the peak-power conversion coefficient η_0 (horizontal, the symbol ⊗ indicates the discontinuity at $\eta_0 = 1$.) and of the reflection coefficient R_ω (vertical). Upper left panel: $s = p = g = 1$; upper right panel: $s = 3$, $p = g = 1$; lower left panel: $s = 1$, $p = 3$, $g = 1$; lower right panel: $s = 1$, $p = 1$, $g = 3$. Regions *A*, *B*, *C* and *D* correspond to the expected optimal performances of the FDNLM. Region *E* represents the projection of our experimental observations using a flashlamp-pumped Nd:YAG oscillator mode-locked by the FDNLM. Other experimental data from different references (see Table 2): open squares (□) for flashlamp-pumped PPT; open circles (○) for PPT lasers pumped by diode lasers; open pentagons (⬠) for diode laser pumped CPT lasers; open stars (☆) for flashlamp-pumped CPT.

crucial because of the limited number of round trips inside the cavity.

- Setting $p = 3$ (with $s = g = 1$) leads to emphasizing the reflected intensity, as shown in the lower left panel, which is important for confining the energy inside the cavity, as it is the case for CPT lasers. In this case the, the best performance is shifted toward the region *C*, where $\eta_0 \in [0.75, 0.88]$ and $R_\omega \in [0.45, 0.70]$.
- In the lower right panel, the importance of the normalized Gaussian shape factor is emphasized by setting $g = 3$ (with $s = p = 1$). The resulting contours show more vertical elongation which means that the condition of minimum deformation can be satisfied for both low and high values of R_ω. The latter fact demonstrates that the FDNLM can be effectively employed with minimum deformation introduced inside the cavity for both PPT and CPT lasers.

Noticeably all maps in Fig. 7 commonly indicate that the best performance of the device is expected for high η_0 values, in the range between 0.75 and 0.88, but not too high. This can be highlighted by going back to Fig. 2 where the η_0 curves for different crystal lengths (1 mm to 10 mm) showing an almost linear behavior of η_0 for values higher than 0.5 and lower than 0.9 where saturation starts and will result in larger deformation of the temporal profile of the laser pulse. Therefore measuring the variation domain of the SH peak-conversion efficiency η_0 shall be our main objective in the next section (Experimental results).

3. Experimental results

In this section we present an experimental investigation about a flashlamp-pumped oscillator, actively and passively mode-locked with both passive-positive and negative mode-locking using FDNLM and TPA components, respectively. The FDNLM consists of a BBO crystal of 3 mm length and a dichroic mirror ($R_\omega = 0.30$) placed at one end of the cavity of a flashlamp-pumped Nd:YAG oscillator. Next to the output mirror we placed a prism to separate the fundamental wavelength and second harmonic beams apart at relatively long distance, where PIN Si photodiodes are placed with a lens to collect all the incoming light. However, since the transmission of the dichroic mirror is about 0.7 for the fundamental i.e. too high to the value of 0.0007 for the second harmonic, we use a neutral density filter (OD 3) to obtain comparable intensities on the photodiodes.

The complete time-evolution of the fundamental and generated second harmonic pulse-trains extracted from the cavity is presented in Fig. 8 (lower panel). The signals (a) and (b) represent the recorded and rescaled energies (i.e. taking into account the transmission factors of all components inserted in the path from the crystal to the detector) of the fundamental and second harmonic pulse-trains respectively. The overall conversion efficiency is deduced by taking the ratio of the second harmonic energy to the sum of both FW and SH energies as depicted by curve (c) in the upper panel of Fig. 8. As aforementioned, η_0 can be calculated by using exponential-expansion fit to the inverse of Eq. (3) as follows:

$$\eta_0 = 528.7678 \times \exp\left(\frac{-\eta_{oc}}{1.3608}\right) - 526.5179 \times \exp\left(\frac{-\eta_{oc}}{1.3451}\right) - 2.24998. \tag{11}$$

The average error of this expression is less than 1% over the whole range. The curve (d) in the upper panel of Fig. 8 represents the estimated peak-conversion efficiency. As one may observe in the lower panel, the two curves show different behaviors with respect to

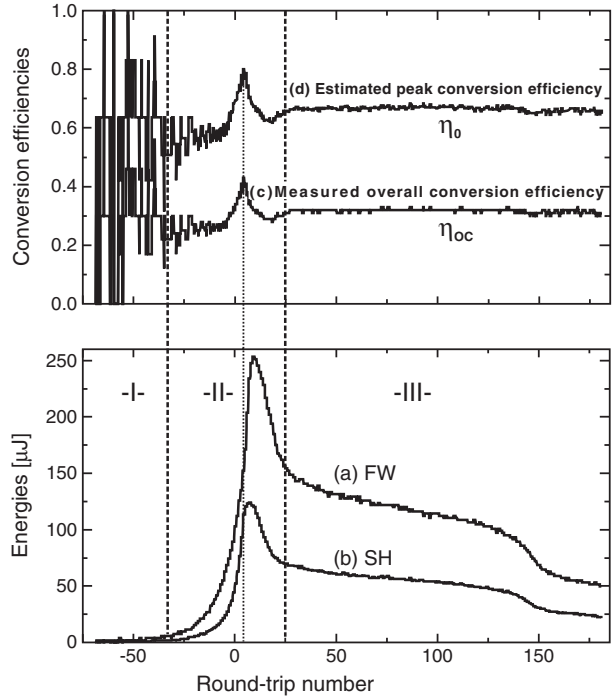

Fig. 8. Lower panel: Pulse-train envelopes measured by a 100 MHz bandwidth oscilloscope with PIN Si photodiodes. The curves (a) and (b) represent the recorded and rescaled energies of the fundamental and second harmonic pulse trains, respectively. Upper panel: curves (c) and (d) show the measured overall conversion efficiency η_{oc} and the estimated peak-power conversion efficiency η_0 (using Eq. (11)), respectively. Note that one round trip time is equal to 10 ns.

the number of round trips (one round trip is about 10 ns). This leads us to divide the pulse train into three time intervals, where the first one shows very low intensities with high fluctuations making the conversion efficiency too difficult to be deduced. After that the intensities become high enough to give a good estimation of the conversion efficiencies as shown in intervals II and III. A relatively large intensity variation of both curves (a) and (b) is observed in the interval II, where the mode-locking process is dominated by the AOML. The second harmonic intensity increases with increasing intensity of the fundamental and so does the deduced η_0 until it reaches the maximum value of about 0.8. A peak-conversion coefficient η_0 of 0.8 is a very high value and the last measurements show that this could be achievable under tight focusing of the TEM_{00} mode inside a relatively thin crystal. Note that the maximum of η_0 does not coincide with the maximum of the second harmonic intensity, which may indicate the beginning of saturation of the generation process inside the crystal. Then both intensities of fundamental and second harmonic pulse trains continue to grow until the second harmonic reaches the maximum first and then the fundamental, which confirms the saturation inside the crystal. After reaching the maximum of the fundamental, all curves decrease together until they reach stable steady values indicating the beginning of the third interval, where a stable operation of mode-locking process is clearly observed due to the hybrid function of both FDNLM and TPA. In this case η_0 stabilizes around the value of 0.68.

Now, projecting our experimental values of η_0 and R_ω (noticing that a stable mode-locking has been observed for different values of R_ω 0.2, 0.25, 0.30, and 0.35) leads us to define a practical operating-domain represented by region *E* in Fig. 7. Region *E* is very close to region *A* (upper left panel) that represents the highest values of the unweighted decision factor. Furthermore, region *E* is even closer to region *B* (upper right panel) where the range of R_ω values is lower than that of *A* which is indeed expected (as mentioned in the previous section) since the limited number of round trips in PPT laser has put more weight on the shortening mechanism. Actually obtaining very high values of $\eta_0 > 0.8$ seems experimentally too difficult and this is the reason that prevents the two regions *E* and *B* from being superimposed. In region *C*, the best performance is shifted to higher R_ω values with a larger choice of η_0.

Table 2
Some reported experimental data of both η_0 and R_ω for successful mode-locking by means of an FDNLM. Note that CPT, PPT, FLP, and DP stand for continuous pulse-train, pulsed pulse-train, flashlamp pumping, and diode pumping, respectively.

Ref	η_0	R_ω	Laser medium; type/pumping; SH generator; pulse width
4	(η_{oc}>0.30) >0.64	0.25	Nd:YAG; PPT/FLP; x mm KTP-II; 100 ps
23	0.73	0.77	Nd:YAG; PPT/DP; 3 mm KTP-II; 41 ps
23	0.73	0.77	Nd:YAG; PPT/DP; 3 mm KTP-II; 42/32 ps
23	0.73	0.69	Nd:YAG; PPT/DP; 3 mm KTP-II; 45 ps
23	0.73	0.69	Nd:YAG; PPT/DP; 3 mm KTP-II; 45/29 ps
23	0.73	0.65	Nd:YAG; PPT/DP; 3 mm KTP-II; 33 ps
23	0.37–0.51	0.77	Nd:YAG; PPT/DP; 5 mm BBO-I; 31/26 ps
23	0.37–0.51	0.69	Nd:YAG; PPT/DP; 5 mm BBO-I; 32/25 ps
24	(η_{oc} = 0.38) 0.75	0.24	Nd:YAP; PPT/FLP; 20 mm LiIO; 15 ps
25	0.80	0.25	Nd:YLF; PPT/FLP; 15 mm LBO-I; 13 ps
26	(η_{oc} = 0.10) 0.26	0.78 (optimum)	Nd:YAG; CPT/DP; 15 mm LBO-I; 10 ps
27	(η_{oc} = 0.10) 0.26	0.775	Nd:YLF; CPT/cw FLP; 15 mm LBO-I; 13 ps

In order to reinforce our point of view we have looked at other available experiments where successful mode-locking with a FDNLM installed as an output coupler and both parameters η_0 and R_ω are reported. These data are listed in Table 2 and plotted on Fig. 7 where the results of PPT and CPT lasers are represented by different symbols. Almost all results of flashlamp-pumped PPT lasers (open squares) are situated within the region *E* which is in accordance with our observations [4,24,25]. Diode-pumped PPT lasers (open circles) are shifted to higher values of R_ω and get closer to region *C*, which indicates that the pumping energies are mostly lower than the ones obtained with flashlamps [23]. Finally, the pumping level in CPT lasers is too low and so is their conversion coefficient η_0 as shown in Fig. 7 [26,27]. Tracking the contours in the lower right corner of the panels points out to the good matching with the experimental data, and leads us to conclude that the FDNLM can be well employed as an output coupler. Consequently, these facts clearly demonstrate the validity of our method to determine the best choice of the physical parameters η_0 and R_ω of the FDNLM device either in PPT or in CPT lasers with attention to the pumping technique.

4. Conclusion

We have presented a detailed post-model analysis of the FDNLM used as passive-positive feedback element in an Nd:YAG laser cavity. Starting from the Stankov model, we deduced a certain number of figures of merit that allow quantifying and optimizing the operation of the device. The calculated parameters could be successfully confronted to experimental measurements from an operating system. Moreover this work shows the capacity of the post-model analysis to highlight the processes alongside the physical model, as well as to clarify our perception about the device functioning that could be easily generalized to the different versions/schemes of this device [28–32] and furthermore to the other mode-locking techniques.

Acknowledgments

A.A.M. acknowledges the Syrian Atomic Energy Commission and the Belgian Fund for Scientific Research (F.R.S.—FNRS) for financial support. D.L. acknowledges the Belgian Fund for Agricultural and Industrial Research (FRIA). Y.C. and A.P. are Research Associate and Research Director, respectively of the Belgian Fund for Scientific Research. A.A.M. thanks the Director of AECS Prof. I. Othman for his encouragement.

References

[1] U. Keller, Advances in lasers and applications, in: D.M. Finlayson, B.D. Sinclair (Eds.), Proceedings of the 52nd Scottish Universities Summer School in Physics, IOP Pub, Bristol, 1999, p. 83.
[2] W. Koechner, Solid-State Laser Engineering, sixth ed.Springer Verlag, Heidelberg, 1999.
[3] K.A. Stankov, Appl. Phys. B 45 (1988) 191.
[4] K.A. Stankov, J. Jethwa, Opt. Commun. 66 (1988) 41.
[5] K.A. Stankov, Appl. Phys. B 52 (1991) 158.
[6] I. Buchvarov, S. Saltiel, K.A. Stankov, D. Georgiev, Opt. Commun. 83 (1991) 65.
[7] V.G. Dmitriev, G.G. Gurzadyan, D.N. Nikogosyan, Handbook of Nonlinear Optical Crystals, third ed.Springer Verlag, Heidelberg, 1999.
[8] A. Agnesi, E. Piccinini, G.C. Reali, C. Solcia, Opt. Lett. 22 (1997) 1415.
[9] V. Kubeček, V. Couderc, B. Bourliaguet, F. Louradour, A. Barthélémy, Appl. Phys. B Lasers Opt. 69 (1999) 99.
[10] A.A. Mani, Ph. Hollander, P.A. Thiry, A. Peremans, Appl. Phys. Lett. 75 (1999) 3066.
[11] A.A. Mani, L. Dreesen, Ph. Hollander, C. Humbert, Y. Caudano, P.A. Thiry, A. Peremans, Appl. Phys. Lett. 79 (2001) 1945.
[12] J. Yu, D. Grando, L. Tartara, V. Degiorgio, Opt. Commun. 260 (2006) 257.
[13] A.A. Mani, Z.D. Schultz, Y. Caudano, B. Champagne, C. Humbert, L. Dreesen, A.A. Gewirth, J.O. White, P.A. Thiry, A. Peremans, J. Phys. Chem. B 108 (2004) 16135.
[14] K.A. Stankov, Appl. Opt. 28 (1989) 942.
[15] J.R.M. Barr, Opt. Commun. 70 (1989) 229.
[16] C.R. Huo, Z.H. Zhu, Opt. Commun. 79 (1990) 328.
[17] V.P. Petrov, K.A. Stankov, Appl. Phys. B 50 (1990) 409.
[18] K.A. Stankov, V.P. Tzolov, M.G. Mirkov, Opt. Lett. 16 (1991) 639.
[19] J.R.M. Barr, Opt. Commun. 81 (1991) 215.
[20] I. Buchvarov, G. Christov, S. Saltiel, Opt. Commun. 107 (1994) 281.
[21] G. Toci, M. Vannini, R. Salimbeni, Opt. Commun. 143 (1997) 156.
[22] O.V. Chekhlov, V.A. Zaporozhchenko, J. Opt. Soc. Am. B 15 (1998) 210.
[23] A. Agnesi, S. Dell'Acqua, G.C. Reali, J. Opt. Soc. Am. B 16 (1999) 1236.
[24] K.A. Stankov, V. Kubecek, K. Hamal, Opt. Lett. 16 (1991) 505.
[25] K.A. Stankov, Appl. Phys. Lett. 58 (1991) 2203.
[26] G. Cerullo, M.B. Danailov, S. De Silvestri, P. Laporta, V. Magni, D. Segala, S. Taccheo, Appl. Phys. Lett. 65 (1994) 2392.
[27] M.B. Danailov, G. Cerullo, V. Magni, D. Segala, S. De Silvestri, Opt. Lett. 19 (1994) 792.
[28] P.K. Datta, S. Mukhopadhyay, G.K. Samanta, S.K. Das, A. Agnesi, Appl. Phys. Lett. 86 (2005) 151105.
[29] S.J. Holmgren, V. Pasiskevicius, F. Laurell, Opt. Express 13 (2005) 5270.
[30] J.H. Lin, K.H. Lin, W.H. Yang, W.F. Hsieh, Opt. Express 13 (2005) 6323.
[31] A. Ray, S.K. Das, S. Mukhopadhyay, K. Datta, Appl. Phys. Lett. 89 (2006) 221119.
[32] J. Yu, Appl. Phys. Lett. 89 (2006) 181107.